*Article*

*J. Mex. Chem. Soc.* **2010**, *54(1),* 7-17

ISSN 1870-249X

# Spectroscopic and Mechanical Studies on the Fe-based Amorphous Alloy 2605SA1

Agustín Cabral-Prieto,[1*] Juan Antonio Contreras-Vite,[2a] Irma García-Sosa,[1] Noel Nava,[3] and Federico García-Santibáñez[2b]

[1] Instituto Nacional de Investigaciones Nucleares, Departamento de Química, Carretera México-Toluca S/N. La Marquesa, Ocoyoacac. C.P. 52750, México. agustin.cabral@inin.gob.mx, Phone: (+) 53297200. FAX: (+) 53297301.

[2] Facultad de Ciencias, Universidad Autónoma del Estado de México. El Cerrillo Piedras Blancas, Toluca, Edo. de México, tony_jv@hotmail.com, fegasa@uaemex.mx.

[3] Instituto Mexicano del Petróleo, Eje Central Lázaro Cárdenas, 152, Col. San Bartolo Atepehuacan, Gustavo A. Madero, C.P. 07730 México D. F. tnava@im.mx.

Received November 10, 2009; Accepted March 19, 2010

**Abstract.** The Vickers micro-hardness of this alloy was unusually dependent on the heat treatment from 300 to 634K, inferring important micro-structural changes and the presence of amorphous grains before its phase transition. Once the alloy is crystallized, the micro-hardness is characteristic of a brittle alloy, the main problem of these alloys. Within the amorphous state, other properties like free-volume, magnetic states and Fe-Fe distances were followed by PALS and MS, respectively, to analyze those micro-structural changes, thermally induced, which are of paramount interest to understand their brittleness problem.
**Keywords:** Amorphous alloys, Mössbauer spectroscopy, annihilation of positrons, free-volume, defects, micro hardness, brittleness.

**Resumen.** La microdureza Vickers de esta aleación presentó una tendencia inusual entre 300 y 634 K, a partir de lo cual se infieren cambios micro-extructurales importantes y la presencia de granos amorfos antes de ocurrir su transformación de fase. Una vez cristalizada la aleación, la microdureza es característica de una aleación fragilizada, el principal problema de estas aleaciones. Dentro de su estado amorfo, fueron estudiadas otras propiedades como volumen-libre, estados magnéticos y las distancias Fe-Fe con PALS y MS, respectivamente, para analizar esos cambios micro-estructurales, inducidos térmicamente, lo cual es del mayor interés para entender su problema de fragilidad.
**Palabras claves:** Aleaciones amorfas, espectroscopía Mössbauer, aniquilación de positrones, volumen libre, defectos, micro dureza, fragilidad.

## Introduction

Amorphous metallic glasses have been the research interest of many groups worldwide because of their unique magnetic, high electrical resistance, mechanical and corrosion resistance properties [1]. Since their discovery by Brenner and Riddell in 1946 [2] and particularly since the early 1960s amorphous alloys with soft magnetic properties have been produced for the manufacture of power transformers and motors, among other applications [3-7]. However, this effort has not completely paid off yet. These alloys, nevertheless, can now be produced with extremely soft magnetic properties [8]. Since the first preparation methods allowed the production of thin foils only [1] large applications were not feasible. By the end of the decade of the 1980s the preparation of bulk metallic glasses extended the preparation methods and changed the perspective of the research in this area [9, 10]. For instance, since 1995 [11] hard magnetic amorphous alloys and nonmagnetic amorphous alloys with strong mechanical properties can be produced. Let us point out, however, that these amorphous alloys have an intrinsic mechanical handicap: when they crystallize they become disappointingly brittle. Great efforts have been made to solve this problem of brittleness [12]. As a result of such an effort it is now well known that the elemental composition, the relative atomic size of the alloyed elements, the presence of volumetric defects, the microstructure, among other properties, all together play a role in this problem. As an example of this Y. H. Liu *et al*. [12] spread light on this problem while studying the ternary alloy ZrCuNiAl, which, under certain elemental composition of its elements becomes super plastic at room temperature and can undergo true-strain of more than 160%. This alloy becomes, however, quite brittle in the crystalline state. It has been suggested that the super plasticity of this amorphous alloy arises as a result of the presence of abundant shear bands which are characterized by soft regions of low mass density and surrounding hard regions of high mass density, i. e., a free-volume difference between these regions may predetermine, in part, the property of super plasticity [12]. Here these hard regions will be taken as the amorphous grains.

Along this line of study, the present paper reports the thermal treatment of the Fe-based amorphous alloy 2605SA1 with soft magnetic properties where free-volume, magnetic and mechanical properties were analyzed as a function of temperature by using Positron Annihilation Lifetime Spectroscopy (PALS), Mössbauer Spectroscopy (MS) and Vickers micro hardness ($H_V$).

## Results

### DSC and thermal treatments

The DSC results of an unheated alloy consist of two exothermic peaks located at 764xK and 807xK. The first exothermic peak is generally associated with the glass transition and/or the first crystallization process occurring at $T_g$ = 764 K; the second exothermic peak is associated with the full or second crystallization process occurring at $T_x$ = 807 K. Thus, a shift of 43K between these peaks is established.

On the other hand, Fig. 1 shows a typical thermal treatment where the heating and cooling rates can be observed for the 856K treatment. Generally speaking, while the heating rate was practically constant at 3C/minute with a standard deviation of 0.1 K, the cooling rates varied between ± 0.5 and ±2 K above 623 K, and below 623 K the variations were with ± 0.1 K. The heating and cooling rates used here are generally lower than those reported in the literature, where heating rates of 10 and 20C/minute and very fast cooling rates are commonly reported [15]. The purpose of using heating and cooling rates lower than those reported in the literature was to reduce the damage to the alloy to a minimal degree.

## DRX

Figures 2 and 3 show some selected XRD patterns of the heated sample at different temperatures. It can be observed from Fig. 2 that the alloy remains in its amorphous state after having been treated at 733 K. On the other hand, the XRD pattern of the sample treated at 753 K shows crystalline material. The first crystallization process was shifted to temperatures lower than those detected by DSC of an unheated sample by about 11C. After treating the sample at 773 K the full crystallization process was almost finished (Fig. 2). The XRD pattern of the sample treated at 783 K (not shown) is like the one shown in Fig. 3 where amorphous material is practically absent. That is, a shift of about 25 K between the $T_x$'s of the unheated and several-times-heated samples was established. The $\Delta T = T_x - T_g$ of the several-times-heated sample was not determined under the present experimental conditions.

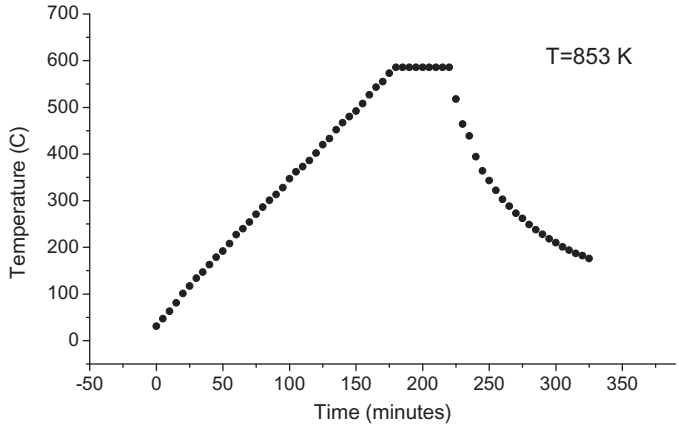


**Fig. 1.** A characteristic thermal treatment of the alloy, where three stages are observed: the linear heating process, the 20 minute time interval where the selected temperature was kept constant, and the nonlinear cooling process.

## PALS

As a result of the annihilation process of positrons in the unheated and heated alloy, three lifetime components were always detected from the recorded lifetime spectra, each component being characterized by a lifetime and a relative intensity. Table 1 shows the estimated parameter values of these components for each selected temperature.

While the shortest lifetime component with $\tau_1$ and $I_1$ is attributed to the annihilation of free positrons in the bulk of the alloy in a delocalized form, the intermediate component with $\tau_2$ and $I_2$ arises from the annihilation of trapped positrons in volumetric voids in the alloy. Finally, the third component with the longest lifetime with $\tau_3$ and $I_3$ is usually associated with the annihilation of positronium (Ps) on the surface of the alloy [16, 17]. The term "positronium" refers to different bound states between a positron and an electron whose lifetimes may vary from 0.5 to 142 ns [18]. For the purpose of the present paper the third lifetime component will not be considered since the surface characteristics of the alloy are not analyzed.

Thus, the parameters of interest are the first and second lifetime components only; these provide information about the atomic micro-structural changes occurring in the bulk

**Table 1.** Positron lifetimes and relative intensities as a function of temperature of the heated 2605SA1 alloy.

| T (K) | $\tau_1$ (ps) | $\tau_2$ (ps) | $\tau_3$ (ps) | $I_1$ (%) | $I_2$ (%) | $I_3$ (%) |
|---|---|---|---|---|---|---|
| 293 | 143 ± 0.6 | 387 ± 5.4 | 1497 ± 17 | 81.5 ± 0.4 | 15.3 ± 0.3 | 3.2 ± .06 |
| 373 | 156 ± 0.5 | 442 ± 8.3 | 1534 ± 24 | 85.5 ± 0.3 | 11.7 ± 0.3 | 2.8 ± .07 |
| 473 | 160 ± 0.7 | 397 ± 5.8 | 1431 ± 15 | 83.4 ± 0.6 | 13.3 ± 0.5 | 3.2 ± .06 |
| 573 | 150 ± 0.5 | 402 ± 5.5 | 1462 ± 16 | 84.4 ± 0.3 | 12.7 ± 0.3 | 2.9 ± .06 |
| 623 | 147 ± 0.8 | 399 ± 8.3 | 1446 ± 22 | 82.7 ± 0.5 | 13.9 ± 0.5 | 3.3 ± .09 |
| 643 | 153 ± 0.5 | 408 ± 6.9 | 1440 ± 17 | 84.3 ± 0.4 | 12.5 ± 0.3 | 3.2 ± .07 |
| 658 | 155 ± 0.5 | 424 ± 7.2 | 1467 ± 18 | 85.3 ± 0.3 | 11.6 ± 0.3 | 3.0 ± .07 |
| 683 | 154 ± 0.5 | 412 ± 7.0 | 1463 ± 20 | 85.8 ± 0.3 | 11.4 ± 0.3 | 2.6 ± .07 |
| 708 | 149 ± 0.7 | 385 ± 7.5 | 1413 ± 20 | 83.4 ± 0.5 | 13.5 ± 0.4 | 3.0 ± .07 |
| 733 | 152 ± 0.6 | 404 ± 6.7 | 1515 ± 23 | 82.5 ± 0.4 | 14.7 ± 0.4 | 2.8 ± .08 |
| 758 | 155 ± 0.7 | 405 ± 7.1 | 1487 ± 25 | 81.7 ± 0.5 | 15.5 ± 0.4 | 2.7 ± .07 |
| 783 | 138 ± 0.8 | 349 ± 4.1 | 1420 ± 16 | 73.6 ± 0.5 | 23.2 ± 0.5 | 3.1 ± .08 |
| 808 | 146 ± 0.9 | 380 ± 4.6 | 1441 ± 18 | 78.4 ± 0.5 | 18.7 ± 0.5 | 2.9 ± .06 |
| 833 | 143 ± 0.7 | 390 ± 5.5 | 1482 ± 20 | 79.3 ± 0.4 | 17.5 ± 0.4 | 3.1 ± .07 |
| 853 | 147 ± 0.1 | 399 ± 8.2 | 1464 ± 24 | 81.0 ± 0.6 | 15.7 ± 0.5 | 3.2 ± .07 |

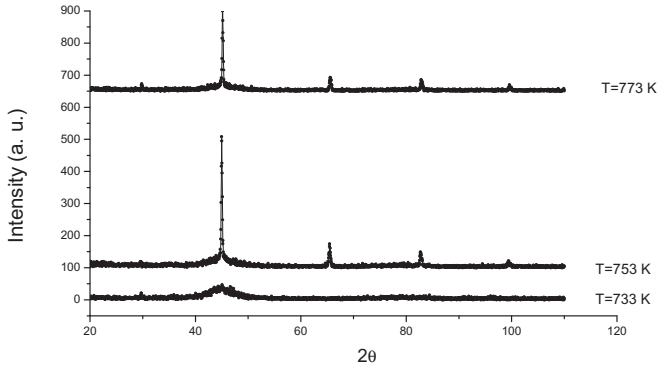


**Fig. 2.** XRD patterns of the alloy in its amorphous and crystalline states as a function of heating temperature.

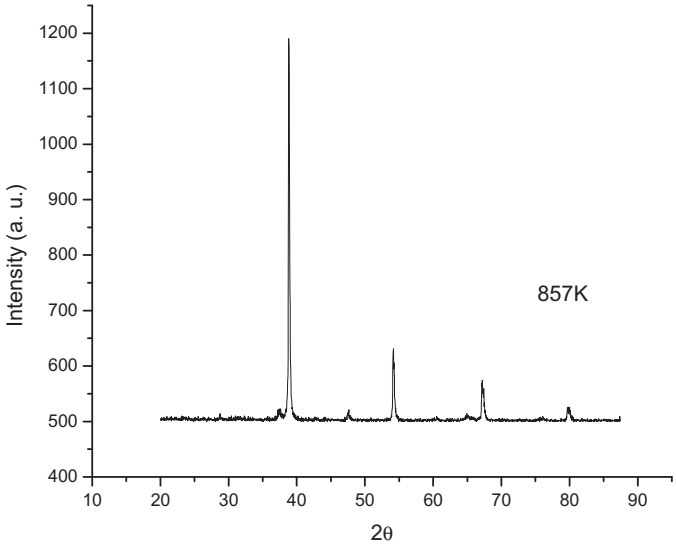


**Fig. 3.** XRD pattern of the crystalline alloy treated at 853K.

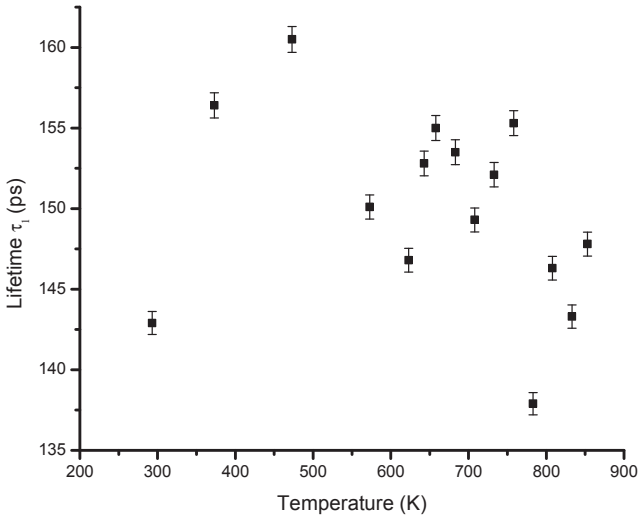


**Fig. 4.** The shortest lifetime of positrons, $\tau_1$, of the amorphous and crystalline states of the alloy 2605SA1 are given as a function of temperature.

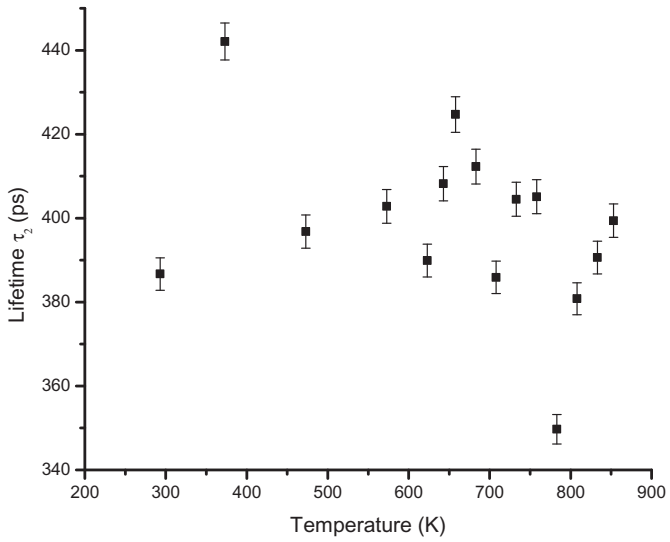


**Fig. 5.** The intermediate lifetime of positrons, $\tau_2$, of the amorphous and crystalline states of the alloy 2605SA1 are given as a function of temperature.

of the alloy as a result of the present thermal treatments. Particularly, the magnitudes of the lifetime constants $\tau_1$ and $\tau_2$ provide information relative to the trapping depth of the defect, the defect size and the electronic density surrounding such defects, respectively. That is, the larger the lifetimes, the lower the electron densities of the defects and/or the larger the lifetimes, the bigger the size of the defects. That is to say, the lifetime of a positron depends on both the electron density at the annihilation site and the defect size [16, 17]. In order to envisage the variations of the defect size and/or the electron density surrounding the defect, Figs. 4 and 5 show the short and intermediate lifetimes as a function of temperature (T). Notice that as a result of the first thermal treatment at 373 K, both $\tau_1$ and $\tau_2$ increase significantly. After this heat treatment, the values of $\tau_1$ decrease slowly and stochastically showing the lowest value at the crystallization temperature $T_x$. Above $T_x$ the values of $\tau_1$ slightly increase. The dependency of $\tau_2$ *vs.* T (Fig. 5) is slightly different from $\tau_1$ *vs.* T (Fig. 4). In this case, the values of $t_2$ remain practically constant, within experimental errors, except at 373 K and at 783 K, where they significantly increase and decrease, respectively. Peculiarly, from the variation of both lifetimes the glass transition or first crystallization process cannot be clearly detected.

## MS

On the other hand, Fig. 6 shows four selected Mössbauer spectra of the unheated and heated alloy. All spectra are typical of Fe-based amorphous alloys [19], each spectrum consisting of a

broadened six-line pattern whose average hyperfine magnetic field (hmf) is $B_{hf}$ = 26.53 T and an average isomer shift δ = 0.07 ± 0.02 mm/s. Such broadening is due to the hmf's distribution arising from atomic disorder in the amorphous state of the alloy [20]. Another characteristic of these spectra is their line-area ratios which deviate from those ratios of a material with total magnetic disorientation, where these ratios are 3:*z*:1:1:*z*:3 with *z* = 2 for lines one to six as depicted in Fig. 6, i. e., a magnetic material without magnetic texture. In the Mössbauer spectrum of the unheated alloy *z* = 2.72, having, therefore magnetic texture; the corresponding *z* value for each spectrum is also given in Fig. 6. This means that a *z* value different from 2 indicates that the sample is already magnetized and some magnetic domains must be aligned in relation to one chosen direction in the absence of an external magnetic field [20, 21]. Thus atomic disorder does not necessarily mean magnetic disorder [22].

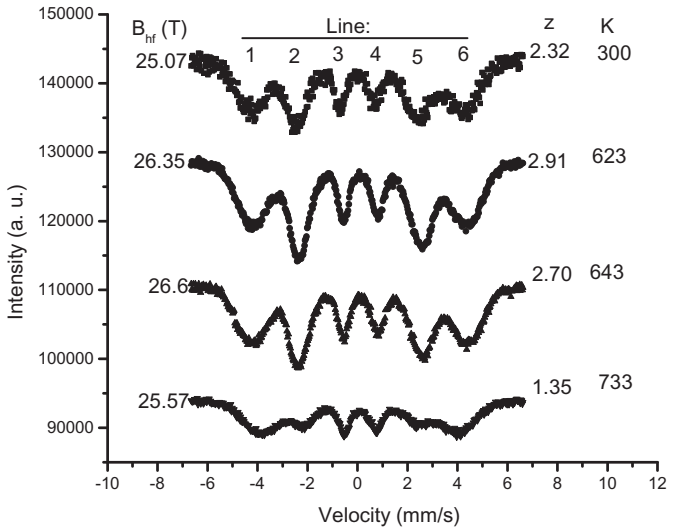


**Fig. 6.** Some Mössbauer spectra of the amorphous heat treated 2605SA1 alloy are shown. Data of temperature, the hmf and the ratio z are also given in the figure.

## $H_V$

Figure 7 shows the micro hardness data as a function of temperature. Whereas the average $H_V$ value of the unheated alloy samples is about 8.6 GPa, the $H_V$ value of the heat-treated samples at 373 K is about 12 GPa. Again the $H_V$ value after the first thermal treatment at 373 K and calculated from Eq. (1) is the highest value of the series with $H_V$ = 12 GPa. Surprisingly, the alloy remained in its malleable state after this first thermal treatment.

$$H_V = 0.1891\left[\frac{F}{(l/5000)^2}\right] \text{ (Kg/mm}^2\text{)}, \qquad (1)$$

In Eq. (1) *F* represents the applied force and *l* is the average length of the diagonal marks produced by the micro diamond indenter.

The subsequent $H_V$ values decrease from 12 to 8.5 GPa almost linearly in the temperature interval of 373-633K, and then presenting two minima with $H_V >>$ 8.5 GPa at about 640 K and at 783 K. Under the present experimental conditions these minima lie within the temperature interval of 633-783 K where the two exothermic processes (at $T_g$ and $T_x$) occur. Interestingly the first minimum of $H_V$ appearing at 640 K may practically be unrelated to the transition at $T_g$, i. e., 640 K is 124 K below $T_g$ as detected from the DSC measurements (section 3.1). The second minimum of $H_V$ appearing at 783 K is, on the other hand, practically the same as it was when the crystallization process ended, i. e., 25 K below from $T_x$ as detected by DSC measurements. The second minimum of $H_V$ is, under the present experimental conditions, clearly correlated to the full crystallization process of the alloy. It is worth mentioning that the alloy was in a high state of brittleness after the eleventh 643 K treatment where still is in the amorphous state, and becoming highly brittle after the eighteenth 783 K treatment where the crystallization process almost had finished.

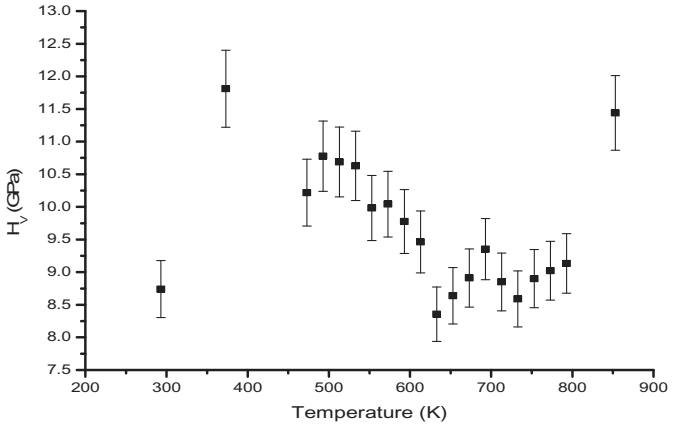


**Fig. 7.** The $H_V$ values as a function of temperature are shown.

## Discussion

### PALS

#### (a) Renormalization of data and mean lifetime $t_m$

As already mentioned in section PALS results, the data of the third lifetime component ($t_3$, $I_3$) will be discarded from this analysis, and in order to do this, a renormalization of the remaining data must be carried out. The new relative intensities are expressed as indicated by expression (2) [18]

$$I_i^* = I_i/(I_1 + I_2), i = 1,2 \qquad (2)$$

Renormalized data are given in table 2. The mean lifetime of the positrons $t_m$ derived from data of Table 2 and estimated

from expression (3) [16, 17, 23] is also given in the last column of Table 2.

$$\tau_m = \tau_1 * I_1 + \tau_2 * I_2 \quad (3)$$

This mean lifetime may represent a measure of the total free-volume available in the bulk of the alloy [23].

On the other hand, the arithmetic average of the shortest lifetime of the heated alloy, $\overline{\tau_1} = \sum_i^{10} \tau_i / 10 = 153$ ps, is slightly higher than the one arising from the unheated alloy, $\tau_1$ = 143 ps (Table 2). Notwithstanding, this means that the electronic density at the annihilation site of positrons in the heated alloy should be lower than that of the annihilation site of positrons in the unheated alloy and/or that the free-volume size at the annihilation site of free positrons is higher than that in the unheated alloy. The most likely situation is that both the electronic density and the free-volume size at the annihilation site affect this average value. Whatever happens, atomic-structural rearrangements occur in the amorphous state as a result of the present mild thermal treatments of the alloy, as detected by PALS. According to this, the magnitude of $\tau_1$ is always greater than that of a defect-free alloy [23] or that of defect-free pure iron having about both the same bulk lifetime $\tau_1 \equiv t_B$ = 106 ± 4 ps [16, 24]. On the contrary, the lifetime of positrons in pure iron containing crystal defects such as mono-vacancies is about 170 ps [16], meaning that the size of the annihilation site as detected in the present case from $\tau_1$ (Table 2) is lower than one atomic vacancy. Deformed interstitial sites could be the candidates of such annihilation sites.

The second lifetime $\tau_2$, associated with the annihilation of positrons in defects bigger than the deformed interstitial sites also show a significant increment after the first thermal treatment at 373K (Fig. 2 and Table 2). Such an increment should be related, as in the preceding case, to a decreasing of the electron density surrounding the defects or to a defect-size increase that is much bigger than the size of a mono-vacancy [16, 24, 25] or to both aspects. If the highest and lowest $\tau_2$ values are statistically removed from the data, the arithmetic average value of the second lifetime is $\overline{\tau_2}$ = 400 ps. The elimination of these $t_2$ values lowers the average value only slightly, going from 404 to 400 ps. PALS and the other measurements, however, suggest that the maximum and minimum $\tau_2$ values, having real physical meaning, are not simply outside the statistics. Thus the larger average lifetime of 404 ps will be retained. After the second thermal treatment at 473 K and up to 733 K there is no significant variation of the $\tau_2$ values. However, after the thermal treatment at $T_x$ = 783K, where the full crystallization process occurs, the lowest value of $\tau_2$ is obtained (Fig. 3); i. e., the significant decrease of $\tau_2$ is associated with the crystallization process of the alloy where large atomic-structural changes occur and the simultaneous decrease of the volumetric defect size as detected by this second lifetime component. The theory of positrons in metals suggests that this decrease in $t_2$ must be associated with a size reduction of the defect rather than with a large decrease of electron density at the annihilation site of positrons [16, 17, 24, 25]. That is, the elemental composition does not change with the transition process nor does the electron density change significantly. This defect-size reduction, together with the new crystalline phases, can be the cause of the high brittleness of the alloy [26]. By increasing the heating temperature above 783 K the values of $\tau_2$ begin to increase, reaching characteristic values of the amorphous state (Fig. 3) thus suggesting that the defect size is restored to its original size.

On the other hand, Fig. 8 shows the variation of the mean lifetime $t_m$ *vs.* $T$. Now, the weighted sum of these lifetimes (Eq. 3) shows the highest value at $T_x$ (Fig. 8) instead of the

**Table 2.** Renormalized PALS data and mean lifetimes given as a function of temperature of the 2605SA1 alloy.

| T (K) | $I_1$ *(%) | $I_2$ *(%) | $\tau_1$ (ps) | $\tau_2$ (ps) | $\tau_m$ (ps) |
|---|---|---|---|---|---|
| 293 | 84.2 ± 0.4 | 15.8 ± 0.3 | 143 ± 0.6 | 387 ± 5.4 | 181 |
| 373 | 87.9 ± 0.3 | 12.0 ± 0.3 | 156 ± 0.5 | 442 ± 8.3 | 191 |
| 473 | 86.2 ± 0.6 | 13.7 ± 0.5 | 160 ± 0.7 | 397 ± 5.8 | 193 |
| 573 | 86.9 ± 0.3 | 13.0 ± 0.3 | 150 ± 0.5 | 402 ± 5.5 | 183 |
| 623 | 85.6 ± 0.5 | 14.3 ± 0.3 | 147 ± 0.8 | 399 ± 8.3 | 182 |
| 643 | 87.0 ± 0.4 | 12.9 ± 0.3 | 153 ± 0.5 | 408 ± 6.9 | 186 |
| 658 | 88.0 ± 0.3 | 11.9 ± 0.3 | 155 ± 0.5 | 424 ± 7.2 | 187 |
| 683 | 88.2 ± 0.3 | 11.7 ± 0.3 | 154 ± 0.5 | 412 ± 7.0 | 184 |
| 708 | 86.0 ± 0.5 | 13.9 ± 0.4 | 149 ± 0.7 | 385 ± 7.5 | 182 |
| 733 | 84.8 ± 0.4 | 15.1 ± 0.4 | 152 ± 0.6 | 404 ± 6.7 | 190 |
| 758 | 84.0 ± 0.5 | 15.9 ± 0.4 | 155 ± 0.7 | 405 ± 7.1 | 195 |
| 783 | 76.0 ± 0.5 | 23.9 ± 0.5 | 138 ± 0.8 | 349 ± 4.1 | 189 |
| 808 | 80.7 ± 0.5 | 19.2 ± 0.5 | 146 ± 0.9 | 380 ± 4.6 | 191 |
| 833 | 81.8 ± 0.4 | 18.1 ± 0.4 | 143 ± 0.7 | 390 ± 5.5 | 188 |
| 853 | 83.7 ± 0.6 | 16.2 ± 0.5 | 147 ± 0.1 | 399 ± 8.2 | 189 |

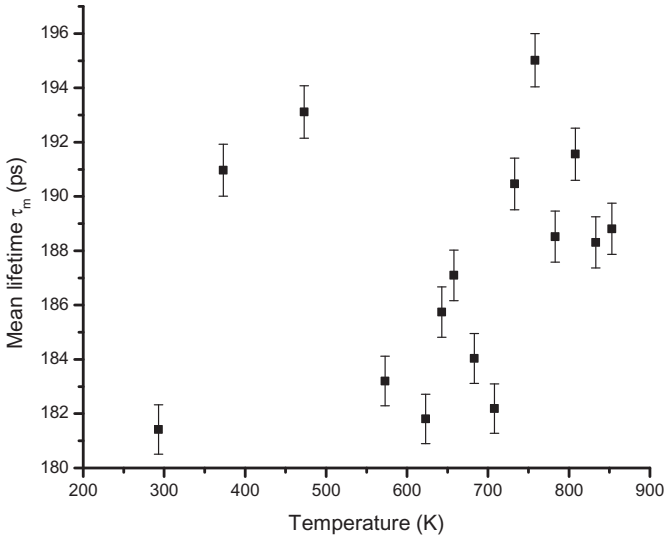


**Fig. 8.** The mean lifetime of positrons, $\tau_m$, as a function of temperature are shown.

minima shown by the un-weighted $\tau_1$ and $\tau_2$ values (Fig. 2 and 3). The highest value of $t_m$ appearing at $T_x$ suggests that at this point of the treatment the alloy contains the maximum amount of free-volume [23]. Table 2 also indicates that the percentage of these volumetric defects increased about two-fold ($I_2$ = 23.9%) with respect to the percentage after treating the alloy at around 600 K's ($I_2$ = 12%) where $\tau_m$ is minimum. As will be shown later, the defect size at the 600K's is greater than the size at 783 K, i. e., the variation of $\tau_m$ as a function $T$ gives evidence that important atomic-structural rearrangements occur in the alloy. In addition to this, the dependency of $\tau_m$ on $T$ is correlated to the other measurements more than are the individual lifetimes $\tau_1$ and $\tau_2$ dependencies on $T$. For instance, this correlation holds for the $H_V$ values (cf. Figs. 7 and 8). The minimal of $H_V$ and $\tau_m$ appearing at around 600K practically coincide in both figures, and the maximum of $\tau_m$ appearing at 758 K is only 25 K above the second minimum of $H_V$. The minimum and maximum of $\tau_m$ might be related to other physical property changes as shown by the Mössbauer results.

**(b) Characterization of defects**

Brandt's simple model describes the trapping and annihilation of positrons in metals where one type of defect is present in such a metal [16, 25, 27]. The model firstly considers that some positrons annihilate in the bulk of the alloy with the annihilation rate $\lambda_b = \tau_b^{-1}$, and secondly, that some other positrons are trapped in volumetric defects with a trapping rate $k$ and eventually annihilate inside them at the rate $\lambda_d = \tau_d^{-1} \circ \tau_2^{-1}$, where $\tau_2$ represents the experimental lifetime given in Table 2.

According to this model the annihilation rate in the bulk is given by [16, 25]

$$\lambda_b = I_1 \lambda_1 + I_2 \lambda_2, \quad (4)$$

being an approximation of $\lambda_B = \tau_B^{-1}$, as already stated for the defect-free annihilation rate. The trapping rate of the positron in the defect is given by [16, 25]

$$k = (I_2/I_1)(\lambda_b - \lambda_d). \quad (5)$$

Finally, this model can be validated by equating the following relation [16, 25]:

$$\tau_1 = (\lambda_b + \kappa)^{-1}. \quad (6)$$

Independently of this model the electronic density in the bulk and surrounding the defects can be estimated from [18, 27]

$$n_i = (\lambda_i - 2)/134 \text{ (a. u.), with } i = b \text{ or } d \quad (7)$$

The derived constants $(\lambda_b, k, n_b, n_d)$ from the above expressions are written in Table 3. As shown from this Table the values of $\lambda_b$ do not change except at $T_x$ where it is maximum. Similarly $\lambda_d$ and $k$ have maximum values at $T_x$. The increase of $\lambda_d$ at $T_x$ suggests a decreasing defect size relative to the existing one in the amorphous state. On the other hand, the electron density of the bulk ($n_b$) is one order of magnitude larger than the one surrounding the volumetric defect ($n_d$) as might be expected. An average value of the electron density surrounding the defects in the amorphous state would be $\overline{n}_d = 3.2 \times 10^{-3}$ a. u., and in the crystalline state $\overline{n}_d = 4.8 \times 10^{-3}$ a. u. This minor difference in the electron density surrounding the volumetric defect between the amorphous and crystalline phases shows that the defect size mostly determines the magnitude of the second lifetime, as already stated.

In order to test the validity of the simple model of Brand to present PALS data the shortest lifetime can be estimated from expression (6) by using the data of Table 3. If expression (6) is equated, which is the case, the assumption is valid for the presence of only one type of defect in the alloy. It can be seen from Eq. (6) that the shortest lifetime is affected by the presence of defects. The actual magnitude of $\tau_1$ may depend on these and other considerations. An extended discussion about the magnitude of $\tau_1$ as a result of the presence of defects is given in the literature [28].

On the other hand, the trapping rate $k$ is related to defect concentration $C$ through [25, 27]

$$\kappa = \mu C, \quad (8)$$

where $\mu = nn$ represents the volumetric trapping rate of positrons in the defect, $n = 6.023 \times 10^{23}(d/A)$ is the atomic density of the alloy, with $d$ and A being the mass density and

**Table 3.** Derived data from the simple trapping model of positrons of Brand, and the electronic densities of the bulk and defects given as a function of temperature.

| T(K) | $\lambda_b$ ($ns^{-1}$) | $\lambda_d$ ($ns^{-1}$) | $\kappa$ ($ns^{-1}$) | $N_b$ ($x10^{-2}$ u. a.) | $N_d$ ($\times 10^{-3}$ u. a.) |
|---|---|---|---|---|---|
| 293 | 6.3 | 2. 6 | 0.69 | 3.2 | 4.4 |
| 373 | 5.9 | 2.3 | 0.49 | 2.9 | 2.0 |
| 473 | 5.7 | 2.5 | 0.51 | 2.8 | 3.8 |
| 573 | 6.1 | 2.5 | 0.54 | 3.0 | 3.6 |
| 623 | 6.2 | 2.6 | 0.61 | 3.0 | 4.2 |
| 643 | 6.0 | 2.4 | 0.52 | 3.0 | 3.3 |
| 658 | 6.0 | 2.3 | 0.49 | 3.0 | 2.6 |
| 683 | 6.0 | 2.4 | 0.48 | 3.0 | 3.1 |
| 708 | 6.1 | 2.6 | 0.57 | 3.0 | 4.4 |
| 733 | 6.0 | 2.5 | 0.61 | 3.0 | 3.5 |
| 758 | 5.8 | 2.5 | 0.63 | 2.8 | 3.5 |
| 783 | 6.2 | 2.9 | 1.00 | 3.0 | 6.4 |
| 808 | 6.0 | 2.6 | 0.80 | 3.0 | 4.7 |
| 833 | 6.1 | 2.6 | 0.80 | 3.1 | 4.2 |
| 853 | 6.0 | 2.5 | 0.69 | 3.0 | 3.8 |

the weighted atomic mass of the alloy, respectively, and $\nu = 4\pi r_d D_+$, with $r_d$ and $D_+$ being the defect radius and diffusion constant of the positrons in the alloy [27], respectively. Here it is assumed that defect-defect distance is larger than the defect diameter in such a way that positrons diffuse certain distance before getting trapped in a defect [27]. Note that the values of $k$ in Table 3 are close to each other from 373 to 758 K, i. e., within the amorphous phase; these values, however, are lower than the $k$ value obtained for the unheated sample. Within this temperature interval the concentration of defects then decreases slightly in relation to the relative concentration registered for the unheated sample. This concentration of defects increases at $T_x$, which can be correlated to the increase of $\tau_m$, indicating that at $T_x$ the free-volume is maximum at this temperature even though the size of the defect is the smallest, as inferred from the lowest magnitude of $\tau_2$ at $T_x$.

Some further comments can be given about the variations of $n_b$ and $n_d$. While $n_b$ practically does not change except after the first two thermal treatments and at $T_x$, $n_d$, on the contrary, varies stochastically throughout all the thermal treatments, increasing slightly when the defect size is the smallest, i. e., at $T_x$. The large stochastic variation of $n_d$ is then indicative that atomic-structural changes occur at the neighborhoods of the volumetric defects.

**(c) Size and concentration of defects**

The type and size of the defects in the 2605SA1 alloy are characterized according to Puska and Nieminen's results [24], which consist of the theoretical correlation between the lifetimes of positrons and the number of mono-vacancies of different sizes and geometries in pure metals such as Fe, Al and Mo. Figure 9 shows the plot of their numerical results for pure Fe.

**Fig. 9.** The correlation between the lifetime of positrons and the number of mono-vacancies for pure iron is given according to Puska and Nieminen [23].

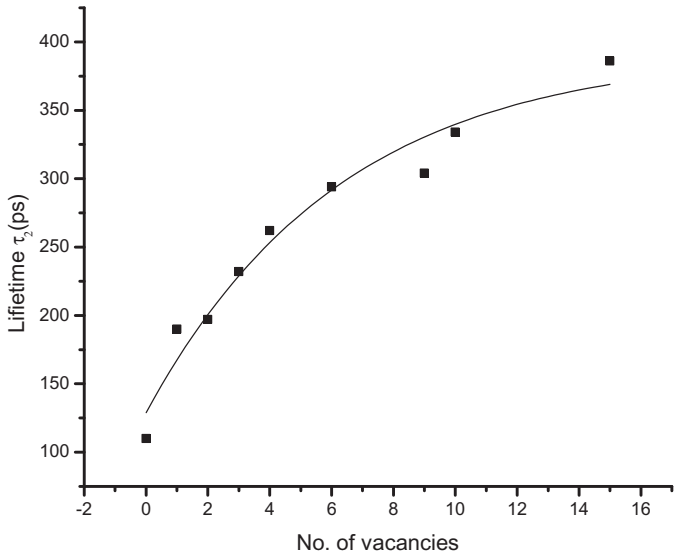


The fundamental concept in which λ depends on the two variables already mentioned, the electron density ($n_-$) and the defect radius ($r_d$) are used to determine these correlations [24]

$$\lambda = 4\pi r_0^2 c \int_0^{r_d} n_+(r) n_-(r) \Gamma[n_-(r)] dr \qquad (9)$$

where $r_0$, c, $n_+(r)$, $n_-(r)$ and $G[n_-(r)]$ are the classical electron radius, the velocity of light, the positron density at site $r$, the electron density at site r and the factor of the electronic enhancement at the positron site, respectively. The numerical method used by Puska and Nieminen is known as the jelium-cavity model [24].

Table 4 shows the experimental $\tau_2$ values and the corresponding types of defects given in terms of clusters of mono-vacancies. These clusters were obtained by matching the lifetimes $\tau_2$ given in Table 4 with those given in Fig. 9 or by interpolation or extrapolation from the data of Fig. 9. The defects of the present alloy consist of clusters from 12 to 18 mono-vacancies. While the smallest clusters appear at $T_x$ = 783K, the largest appear at 373 and 658K. The crystalline material ends up with clusters of about 15 mono-vacancies (Table 4).

Next, the estimation of the defect sizes in the amorphous and crystalline states must be taken as approximate values to the actual defect sizes.

Particularly, the Fe content in the alloy is about 98.84% and the remaining 1.16% is due to alloyed elements such as Cr (0.05%), Mn (0.13%) and Si (0.98 %), as determined by Particle-induced X-ray emission (PIXE) [29]. In this sense, the electron density in which the positrons annihilate differs slightly from that of pure Fe because of the presence of Mn, Cr and Si. The atomic size and the positron affinity ($A_+$) of Cr, Mn, Fe and Si are 125, 137, 124 and 118 pm, and –2.62, –3.72, –3.84 and –6.95 eV [30], respectively. According to the $A_+$ data Si followed by Fe would be the main attracting elements of positrons in the alloy. In addition to this and because the Si atoms are the smallest of all, they could be related to the deformed interstitial sites, as suggested before. The influence of Cr and Mn in the annihilation process of positrons in the alloy may seem insignificant, due also to their low relative concentration of 0.18%, thus reducing the possibility that these elements may contribute to the annihilation process of positrons in the alloy. In this sense the characterization of the type of defects in the alloy may turn out realistic.

Taking into account these considerations, the size of the defects can now be roughly estimated by using the results of Puska and Nieminen for pure Fe [24]. The defects in the alloy are clusters ranging from 12 to 18 mono-vacancies (Table 4). Thus clusters of 16, 12 and 15 mono-vacancies for the amorphous, for the transition process and for the crystalline states, respectively, are considered. Figure 10 shows a cluster of 15 mono-vacancies for the BCC crystalline structure of Fe [24], i. e., all the nine Fe atoms of a unit cell plus the central atoms of the next six neighboring unit cells are removed [24]. Knowing the lattice parameter $a$ of the BCC unit cell for pure

**Table 4.** Type of defects found in the amorphous and crystalline states of the 2605SA1 alloy.

| T(K) | $\tau_2$ (ps) | No. of mono-vacancies |
|---|---|---|
| 293 | 387 | 15 |
| 373 | 442 | 18 |
| 473 | 397 | 15 |
| 573 | 402 | 16 |
| 623 | 399 | 15 |
| 643 | 408 | 18 |
| 658 | 424 | 18 |
| 683 | 412 | 18 |
| 708 | 385 | 15 |
| 733 | 404 | 16 |
| 758 | 405 | 17 |
| 783 | 349 | 12 |
| 808 | 380 | 14 |
| 833 | 390 | 15 |
| 853 | 399 | 15 |

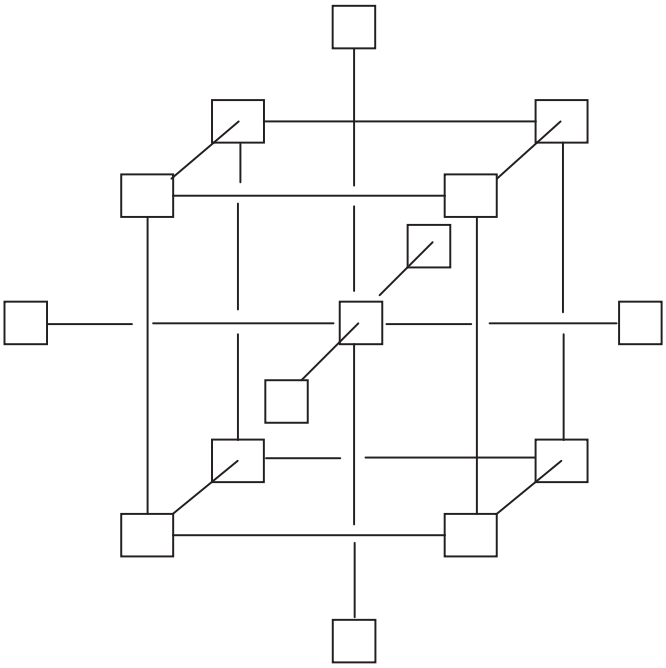

**Fig. 10.** A cluster of 15 mono-vacancies in the BCC crystal structure of α-Fe is shown according to Puska and Nimeinen [23].

iron, which is $a$ = 0.264 nm [24], the cluster radius in the crystalline alloy may be roughly estimated. As shown in Fig 10, the diameter of the cluster is about 2 times that of the unit cell parameter $a$. In this sense the cluster radius would be $r_d = a$, being an approximate value for the size of the defect in the crystalline sate of the alloy. For the amorphous phase these clusters would be different and they probably would be located at any site among the amorphous phase where the cluster form should deviate from that shown in Fig. 10. The size of these amorphous clusters should not, however, deviate much from the previously estimated $r_d$ = 0.264 nm for the crystalline state of the alloy, their size would be ~ 0.282 nm, i. e. a 6.7% larger than those of the crystalline phase.

Thus, according to Eq. (8) the relative concentration of defects can now be estimated from

$$C = k/(4\pi n r_d D_+). \qquad (10)$$

Typical values of $D_+$ for these alloys are ~ 0.31 $cm^2/s$ and $n = 6.023 \times 10^{23}(d/A)$ [24] with $d$ = 7.18 $g/cm^3$ and A = 55.57 g/mol. Thus, $n = 7.78 \times 10^{22}$ atoms/$cm^3$ and $r_d = 0.282 \times 10^{-7}$ cm. With these values a relative value of $C = 8.070^{-8}$ $at^{-1}$ for the unheated alloy is obtained. For the 783 K treated alloy the relative value of $C = 1.57 \times 10^{-7}$ $at^{-1}$, i. e., at the phase transition two things occur: an increase of the number of clusters ($I_2$ or $\tau_m$ increase, Table 2) and a decrease of their size to a radius of ~ 0.21 nm, i. e., 20% lower than the radius for the clusters of 15 mono-vacancies. For the purpose of comparison, consider the relative concentration of defects in melted metals, which is C ~ $10^{-4}$ $at^{-1}$ [31, 32].

## MS

Only four Mössbauer spectra corresponding to the amorphous state of the alloy are shown in Fig. 6. Average values of the hmf and isomer shift, with $B_{hf}$ = 26.53T and δ = 0.07 mm/s, respectively, were determined from these spectra. Variations in the parameter $B_{hf}$ suggest atomic rearrangements affecting the Fe-Fe distances and therefore the size of the free voids [21]. The $B_{hf}$ for each spectrum is given in Fig. 6. The Mössbauer spectrum of the crystalline state, not shown here, arises, on the other hand, from a superposition of spectra and differs completely from those shown in Fig. 6. Different crystalline phases precipitate, giving each one of them a characteristic hmf, which is not studied here.

What is important to emphasize from the Mössbauer spectra shown in Fig. 6 is the following. First, the slight increase of $B_{hf}$ relative to the $B_{hf}$ value measured for the unheated sample may denote a decreasing length between the Fe-Fe distances [21]. According to PALS measurements, and particularly through the variation of $\tau_m$, there is a slight increase of the total free-volume between the 623 and 758K treatments, which is probably correlated to the slight shortening distance of the Fe-Fe distances in this temperature interval as inferred from the increase of the hmf values, as shown in Fig. 6. That is, as the average free voids increase, the Fe-Fe distance decreases.

Second, the area ratios of the six-line patterns, shown in Fig. 6, vary depending on the heat treatments of the alloy. According to Mössbauer theory [20] these area ratio variations result from domain magnetic reorientation with respect to the gamma-ray 14.4 keV direction in the transmission set up

Mössbauer experiment. The domain magnetic orientation can be determined from

$$z = 4\,\mathrm{Sin}^2(\theta)/(1 + \mathrm{Cos}^2(\theta)), \qquad (11)$$

where $z$ is the average area ratio between peaks 2 to 3 and peaks 5 to 4, θ being the angle between the incident gamma-ray of 14.4 keV and the domain magnetic direction in the sample. For $z = 0$, $\theta = 0^0$, meaning that the magnetic domain and the gamma-ray directions are parallel to each other, and for $z = 4$, $\theta = 90^0$ these direction are oriented perpendicular to each other. The corresponding q values for the $z$ values, given in Fig. 6, are $64^0$, $70^0$, $75^0$ and $46^0$, respectively. It should be noticed that the domain magnetic orientation with $\theta = 46^0$ occurs at the 733 K treated alloy, i. e., near the first crystallization process or glass transition, thus suggesting that this magnetic reorientation occurs when the free-volume of the alloy is maximum, as indicated by the variation of $t_m$ in Fig. 8. On the other hand, the domain magnetic orientation with $\theta = 75^0$occurs at 643 K, where the total free-volume of the alloy is minimum. Notice that this minimum appears at the same temperature of the first minimum of the $H_V$ *vs*. $T$ plot, (Fig. 7).

## $H_V$

As indicated in the previous section of $H_V$ results, the two alloy samples of 2.56 $cm^2$ showed the highest value of the $H_V$ data after the first thermal treatment at 373 K. This $H_V$ value is as high as the one obtained at the 853 K treated alloy, after which the alloy was completely brittle. On the contrary, the alloy does not lose its ductility after the first 373 K thermal treatment. The high value of $H_V$ at the start of the thermal treatments may, under the present experimental conditions, be related to an increase of free-volume as detected from PALS (Table 4 and Fig. 8). As can be seen from Table 4, after the first thermal treatment of the alloy the largest cluster of 18 mono-vacancies is obtained, where the total free-volume is relatively high (Fig. 8) and the big size of the cluster may the brittleness of the alloy prevent from occurring even though it possesses a high $H_V$ value after this treatment. Among other things, residual stress is also removed from the alloy after this first thermal treatment.

As can be seen from Fig. 7, the $H_V$ values decrease in the temperature interval 473-653K reaching values of $H_V$ as low as those of the unheated alloy. However, after the 653 K treatment, the alloy still remains in the amorphous state (Fig. 2) but did not have the ductility that was characteristic of the unheated sample, instead, it was already brittle. Although data given in Table 4 indicate that the largest cluster sizes appear at around the 650 K's, the total free-volume is intermediate between the original total free-volume and that detected at $T_x$ (Fig. 8). Now the property of brittleness of the alloy seems to depend only on the variation of the total free-volume which is lower than that detected at the 373 K treatment.

Between 600 and 800 K the $H_V$ data present two minima, one appearing at about 633 and the other at 733 K (Fig. 7). Notice from Fig. 2 that the alloy is still in its amorphous state after treating it at 733 K. Thus, the first minimum of $H_V$ appearing at 633 K (Fig. 7) can be related more to a magnetic reorientation process, already discussed, rather than to the first crystallization and/or glass transition which, under the present experimental conditions, is about 120 K away from 753 K, temperature at which the first crystallization began (Fig 2). According to the DSC results of the unheated sample, the first crystallization process began at 764 K. Such a shift of about 11 K, therefore, occurs as a result of the present thermal treatments on the alloy.

On the other hand, notice from Fig. 7 that at about 783 K, temperature at which the second transition occurs under the present experimental conditions, the $H_v$ values are relatively low and correspond to the second minimum of $H_V$. However, at this stage of the thermal treatment of the alloy, the samples are quite brittle, the cluster size being the smallest with 12 mono-vacancies (Table 4) and their relative concentration being the highest (Table 2 and Fig. 8).

The $H_v$ value of the alloy samples after being treated at 853 K is practically the same as that obtained after the first 373 K treatment, but now this new highest value of $H_v$ does indeed correspond to the high degree of brittleness of the alloy. According to the $\tau_m$ results the brittle state of the alloy possesses a total free-volume just 1.04 times larger than that of the unheated alloy (Table 2), i. e., the total free-volume of the sample seems to be practically the same but with a cluster size that is the smallest. Thus the cluster size and the crystalline phases may now be responsible for the property of brittleness of the alloy.

In particular, the Vickers's micro-hardness is inversely related to the grain size $d$ of a crystalline material as [21]

$$H_V = \sigma_i + k_f d^{-1/2}, \qquad (12)$$

where $s_i$ is the intrinsic resistance to deformation of the material and represents the minimum energy required to move a dislocation. If the Hall-Petch relation (Eq. 12) applied to the amorphous state, the constant $s_i$ would be related to the movement of a shear band instead of a dislocation. The analogous case for the grain concept in the amorphous state would be the material of high mass density enclosed by those shear bands as stated in the introduction. $k_f$ in Eq. (12) would represent the constant that describes the start of movement of such a shear band on a particular material. The intention in the present paper is to make an extension of Eq. (12) to the amorphous state. In this sense, the decreasing tendency of $H_V$ occurring from 373 to 653 K might be associated with the variation of the amorphous grain [12]. Whether a normal or an inverse Hall-Petch relation exists in the present case cannot be assessed from Fig. 7, but the manual test of brittleness which increases with an increase of the temperature treatment, from 373 to 653K, indicates a normal Hall-Petch relation, i. e., the grain size increases as the $H_V$ decreases. It has been

the research subject of several groups to look for the inverse Hall-Petch relation in nano-crystalline alloys with crystal size below and above the 25 nm [21]. This inverse relation would partially solve the brittleness problem. For instance, it has been observed that by controlling the grain size below this 25 nm value, an inverse Hall-Petch relation holds for certain pure metals [21]. In such a case, the grain size reduces as the $H_V$ values decrease.

Returning to the present analysis, Tong et al. [23], reporting a study on the heat treated FeSiB alloy where $H_V$ and PALS results are presented, show the correlation among $H_V$ (GPa), $d$ (nm) and $\tau_m$ (ps), (see Fig. 5 of their paper). In that Figure a normal Hall-Petch relation is shown where $H_V$ decreases as $d$ increases. Under these circumstances the $\tau_m$ values also decrease as $d$ increases. Although fewer $\tau_m$ data points are presented in Fig. 8 in the region of interest to be matched with the data points of $H_V$ in Fig. 7, a decreasing tendency of $\tau_m$ is also observed from 373 to 653K (Fig. 8). In this sense, within this temperature range the amorphous grain size would increase, and a normal Hall-Petch relation is then predicted for the present data.

## Conclusions

The defects in the Fe-based amorphous alloy 2605SA1 consist of small free voids with radii that range from 0.21 to 0.32 nm, as estimated from PALS measurements. The location site of the voids is unclear but they are possibly located in the inter-grain regions. The smallest sizes of these voids appear at the transition temperature $T_x$. Besides, the $T_x$ appears about 25 K lower than that detected by DSC measurements of an unheated alloy sample. This temperature shift must arise as a result of the several thermal treatments which the sample was exposed to.

By using the simple trapping model of positrons in metals, the trapping rate of positrons in the small free voids and the relative concentrations of these voids were estimated, i. e., $C = 8.08 \times 10^{-8}$ at$^{-1}$ for the unheated alloy and $C = 1.57 \times 10^{-7}$ at$^{-1}$ for crystalline state at $T_x$, the latter $C$ value being the largest relative concentration of voids in the sample. The electron densities in the bulk and that around the free voids were estimated where the latter is one order of magnitude smaller than the former. While the electronic density of the bulk was practically constant throughout all thermal treatments of the alloy, the electron density surrounding the voids changed and increased slightly at $T_x$, thus suggesting detectable atomic structural changes as a result the present mild thermal treatments.

Magnetic reorientations in the amorphous state of the alloy were also followed by MS. Domain magnetic reorientations and free-volume variations seem to occur concomitantly. For instance, when the magnetic orientation of the sample, relative to the gamma-ray direction, is maximum, i. e., $\theta = 75^0$'s, the free-volume of the alloy is minimum or comparable to the existing one in the unheated alloy. Similarly, when the magnetic orientation is minimum, i. e., $\theta = 46^0$, the free-volume is relatively high as compared with that detected at the transition temperature $T_x$.

Hence, the measured property of brittleness of the alloy after the heat treatments within the amorphous state could be related in part to the detected free-volume changes occurring at the sample. This property of brittleness of the amorphous state may also be attributed to an increase of the amorphous grain following a normal Hall-Petch relation.

## Experimental Section

The Fe-based amorphous alloy 2605SA1, Lot 3199544 was produced by melt-quenching and was provided by J. Jordan and Dr. Hasegawa from Metglass Inc. Co. in the USA. This alloy consists of a sheet 25 mm thick, 17 cm wide and 2 meters long. Small samples of different sizes, having been cut from this long sheet, were simultaneously temperature treated between 373 K and 853 K. The heating rate was 3C/minute, and the selected temperature being maintained for 20 minutes before cooling. The ASA VF-1000 furnace, connected to a vacuum system ($10^{-6}$-$10^{-7}$ torr), and to the S8-VF temperature controller were used for these thermal treatments.

Differential Scanning Calorimeter (DSC) of an unheated sample was carried out to determine the phase transition temperatures of the alloy by using a heating rate of 3C/minute. A DSC ENETZSCH apparatus, model STA 409 PC LUXX was used for this purpose.

For PALS experiments, an arrangement of six sheets of 1.0cm × 0.5cm and the radioactive $^{22}$NaCl source was prepared as follows: a micro drop of an aqueous solution containing 15 mCi of $^{22}$NaCl carrier free was deposited on a Nickel foil 3 mm thick 0.6 cm long and 0.3 cm wide. The aqueous content was evaporated by using infrared light until dryness. The Nickel foil was then folded keeping the surface impregnated with $^{22}$NaCl inside this folding. The folded foil was then sandwiched with three 1.0 cm long by 0.5 cm wide sheets of the alloy at each side. This arrangement was fixed by covering it with an aluminum foil; it was then put inside a Pyrex tube, which was connected to a vacuum system ($10^{-4}$ torr). In this way, the sample was evacuated for 90 minutes before the tube was sealed off. A fast-fast coincidence system with a resolution function of 0.29 ns and a 50 ns time window was used to record the lifetime spectra of the unheated and heated sample. The lifetime spectra were analyzed by using the Positronfit program [13] and a home-made program. For the thermal treatments the sealed tube with the sample and four more alloy sheets were put inside the furnace and heated up to the desired temperature, as already indicated. The dimensions of the four sheets were 1.6 cm long by 1.6 cm wide. On of these sheets was always used to record the Mössbauer spectra of the unheated and heated sample. A constant acceleration spectrometer with a $^{57}$Co/Rh source was used and the Mössbauer spectra were analyzed by using the Normos program [14]. The isomer shifts of the resulting spectra are referred to the center of the Mössbauer spectrum of natural iron.

Similarly, another 1.6 cm long by 1.6 cm wide sheet was used to record the X-ray diffraction (XRD) patterns of the unheated and heated sample. The Siemens D5000 apparatus coupled with a CuKa X-ray source was used for this purpose. The two remaining sheets of 1.6 cm long by 1.6 cm wide were used to doubly measure the $H_V$ values of the unheated and heated samples. The micro hardness Beuheler 5101 Micromet apparatus with a load of 50g/15s was employed. Five indentations on each side of the unheated and heated sheets were made. The reported $H_V$ data therefore arise from 20 indentations.

## Acknowledgements

We are grateful to J. Jordan and Dr. R. Hasegawa from Metglass Inc. Co. in the USA for providing us with the 2605SA1 alloy sample.

## References

1. Linderoth, S. *Hyperfine Interactions* **1991,** *68*, 107-118.
2. Brenner, A.; Riddell G. *J. Res. Natl. Bur. Stand*. **1946**, *37*, 31-34.
3. Luborsky, F. E. IEEE *Trans. Mag.* **1978,** *14*, 1008-1012.
4. Klement, W.; Wilens, R. H.; Duwez P. *Nature* **1960,** *187*, 869-870.
5. Mader, S.; Nowick, A. S. *Appl. Phys. Lett*. **1965**, *7***,** 57-59.
6. Tsuei, C. C.; Duwez, P. *J. Appl. Phys.* **1966**, *37*, 435.
7. Duwez, P.; Lin, S. C. H. *J. Appl. Phys.* **1967,** *38,* 4096-4097.
8. Huang, D. R.; Li, J. C. M. *Mat. Sci. and Eng,* **1991**, *A133*, 209-212.
9. Kui, W. H.; Greer, A. L. Turnbull, D. *Appl. Phys. Lett.* **1984**, *45*, 615-616.
10. Wang, W. H. *Progress in Materials Science* **2007**, *52*, 540-596.
11. Ram, S. *Current Science*, **2004**, *86(6)*, 832-838.
12. Liu, Y.; Wang, H. G.; Wang, R. J.; Zhao, D. Q.; Pan, M. X.; Wang,W. H. *Science* **2007**, *315(9),* 1385-1388.
13. Kirkgaard, P.; Eldrup, M. *Comput. Phys. Commun*. **1972** *3*, 240-255.
14. Brand, R. A. *User´s Guide, Wissenschaftlich Elektronic GmbH* **1992**.
15. Nakajima, T.; Nagami, I.; Ino, H. *J. of Materials Science Lett.* **1986,** *5*, 60-62.
16. Hautojärvi, P.; Corbel, C. In *Proceedings of the International School of Physics "Enrico Fermi": Positron Spectroscopy of Solids, Editado* A. Dupasquier y A. P. Mills Jr.; Technical Editor P. Papali, IOS y Ohmsha. **1995**, 491-580.
17. M. Nieminen, R.; Manninen M. J. In *Topics in Current Physics: Positrons in Solids* (12), Edited by P. Hautojärvi, 1ª ed., Springer-Verlag **1979**, 145-195.
18. Wen-Deng, L.; Xiong, Y.; Lung, C. W.; Wang, S. H.; Guo, J. T. *Materials Science Forum* **1995,** *175-178,* 339-342.
19. Cabral-Prieto, A.; García-Santibáñez, F.; López, A.; López-Castañares, R.; Olea-Cardoso, O. *Hyperfine Interactions* **2005,** *161*, 69-81.
20. Vertés, A.; Korecz, L.; Burger, K. *Mössbauer Spectroscopy*, Elsevier Scientific, Budapest, **1979.**
21. Li, J. M.; Quan, M. X.; Hu, Z. Q. *Appl. Phys. Letters* **1996**, *69(11)*, 1559-1561.
22. Gubanov, A. I. *Sov. Phys.-Solid State* **1960,** *2*, 468-471.
23. Tong, H. Y.; Ding, B. Z.; Wang, J. T.; Lu, K. *J. Appl. Phys*. **1992**, *72(11),* 5124-5129.
24. Puska, M. J.; Nieminen, R. M.; *J. Phys. F: Met. Phys*., **1983**, 13, 333.
25. Eldrup, M.; in *Defects in Solids*, Edited by A. U. Chadwick, M. Terenzi, Plenum Publishing Corporation **1986,** 145-178.
26. Elliott, S.R., *Physics of amorphous materials* 2ª ed., Longman scientific and technical, New York, **1989**.
27. Brandt, W. *Appl. Phys*., **1974**, 5**,** 1-23.
28. Cizek, J.; Prochazka, I.; Kocik J. ; Keilova, E. *Phys. Status Sol*. (a) **178** (**2000**) 651-662.
29. Contreras-Vite , J. A., *Tratamiento térmico de la aleación amorfa 2605SA1. Análisis de sus defectos y microdureza* **2008**, Tesis de Licenciatura en Física. UAEM. Toluca, México.
30. Nieminen, R. M.; In: *Positron Spectroscopy of Solids*, Edited by A. Dupasquier and A. P. Mills Jr. IOS press **1995**, 443-489.
31. McKee, B. T. A.; Jost, A. G. D.; MacKenzie, I. K. *Can. J. of Phys*.,**1972**, 50**,** (5) 415-420.
32. Seeger, A. *J. Phys. F: Metal Phys.***1973**, 6, 248-294.